EES Solar

PAPER

View Article Online
View Journal | View Issue

Cite this: *EES Sol.*, 2025, **1**, 632

The role of $MAPbI_3$ hydrate in triple mesoscopic stack minimodules: the key to elongating outdoor lifespan†

Susana Iglesias-Porras, *[a] Amy Neild, [a] Johannes Gausden,[b] Mathew Barraclough[b] and Elizabeth A. Gibson *[a]

Despite their promising performance and low-cost fabrication, perovskite solar cells (PSCs) face significant commercialization challenges due to their environmental instability, limiting their long-term durability. While encapsulation strategies improve stability, no existing solution demonstrates PSCs can last at timescales comparable to market-dominant silicon photovoltaics. This study explores an alternative approach: complementing effective encapsulation with maintenance actions. To enable such interventions, it is essential to understand how environmental factors influence device performance in real-world conditions. To do so, we fabricated triple mesoscopic stack (TMS) $MAPbI_3$ perovskite solar cells and mini-modules, encapsulated them with different materials, and deployed them for outdoor testing in North Yorkshire, UK, across different seasons. We observed that under the high relative humidity (RH) experienced on site, devices showcased an increase in open-circuit voltage (V_{OC}), temporarily enhancing power output. Laboratory experiments using XRD confirmed this V_{OC}-to-RH relationship to be driven by the reversible formation and dissolution of $MAPbI_3$ monohydrate, which facilitated charge extraction at the perovskite/carbon interface. While prolonged exposure led to degradation, partial recovery was achievable through temperature- or vacuum-induced water removal. Notably, Parylene-C encapsulation effectively prevented irreversible degradation under high humidity and temperature conditions. These findings reveal that V_{OC} and short-circuit current density (J_{SC}) variations can serve as *in situ* early indicators of reversible hydration-induced degradation, enabling preventative maintenance before power loss occurs. These findings support circular economy principles and, alongside advances in encapsulation, can increase PSC durability, bringing the technology closer to commercial viability.

Received 15th May 2025
Accepted 10th July 2025

DOI: 10.1039/d5el00076a

rsc.li/EESSolar

Broader context

Perovskite solar cells (PSCs) are among the most promising next-generation photovoltaic technologies, offering high efficiencies and low production costs. However, their limited long-term stability under real-world conditions remains a major barrier to commercialization, threatening their potential contribution to global renewable energy goals. Our study addresses this challenge by introducing a preventative maintenance strategy informed by *in situ* performance monitoring—an underexplored yet impactful approach to enhancing PSC resilience. By analyzing triple mesoscopic stack $MAPbI_3$ solar cells and minimodules deployed outdoors in the UK across seasonal cycles, we reveal that early-stage moisture exposure can transiently improve performance through reversible open-circuit voltage increases linked to monohydrate formation. Rather than viewing these interactions solely as degradation pathways, we show they can serve as diagnostic signals for impending failure. We identify relative humidity-driven changes in V_{OC} and J_{SC} as early indicators and demonstrate that timely interventions—such as vacuum or thermal treatments—can restore performance. Moreover, we validate Parylene-C encapsulation as an effective barrier against irreversible damage. By integrating real-world data, protection strategies, and maintenance protocols, our work advances a practical roadmap for PSC durability. These insights support global efforts to develop stable, scalable, and commercially viable solar technologies critical for a sustainable energy future.

Introduction

Perovskite solar cells (PSCs) have emerged as a leading candidate among next-generation photovoltaic (PV) technologies, achieving record power conversion efficiencies matching those of silicon-based solar cells.[1] Among various architectures, the triple mesoscopic stack (TMS) has garnered significant attention due to its scalability, material availability, low cost, and

[a]*Energy Materials Laboratory, School of Natural and Environmental Science, Newcastle University, Newcastle Upon Tyne, NE1 7RU, UK. E-mail: susana.iglesias-porras@newcastle.ac.uk; elizabeth.gibson@newcastle.ac.uk*

[b]*School of Engineering Newcastle University, Newcastle Upon Tyne, NE1 7RU, UK*

† Electronic supplementary information (ESI) available. See DOI: https://doi.org/10.1039/d5el00076a

improved device longevity.[2] The carbon counter electrode, in particular, has contributed to enhanced stability owing to its hydrophobic properties.[2] Despite lower efficiencies than more expensive alternatives, TMS have shown significant progress, with small cells reaching 17.48% and mini modules achieving 12.87% efficiency for an active area of 60.08 cm^2.[3,4] However, PSCs still face challenges in matching the 25-year lifespan of silicon-based devices, primarily due to their sensitivity to environmental factors such as oxygen, UV light, temperature, and moisture.[5]

A major area of focus for improving the longevity of PSCs is the development of effective encapsulation materials. To date, no single material has fulfilled all the requirements for optimal encapsulation.[5] These include exceptionally low oxygen and water vapor transmission rates (OTR: 10^{-4}–10^{-6} cm^3 per m^2 per day, WVTR: 10^{-3}–10^{-6} cm^3 per m^2 per day), the ability to withstand high temperatures, chemical stability, resistance to interactions with device components, and other factors such as strong adhesion, thermal compatibility, flexibility, UV resistance, scalability, and cost-effectiveness.[5] Currently, the most suitable approach involves using a combination of materials, including blanket encapsulation and edge sealing with a cover glass.[5] Yet, despite predictions that PSCs could achieve operational lifespans of up to 30 years,[6,7] outdoor stability studies have shown much shorter lifespans, with the longest lasting devices reaching T_{80} in a year or less under real operating conditions.[8–11]

Given these challenges, it is becoming increasingly clear that achieving silicon-like durability for PSCs may be more difficult than initially anticipated. As a result, adopting a circular economy approach—designing for recyclability, extending product lifespans through maintenance, and enabling material recovery at the end of life—could offer a promising solution. Circularity emphasizes proactive maintenance to detect early signs of degradation, thereby preventing irreversible failure. To implement this effectively, it is crucial to understand the outdoor degradation processes of PSCs and their timelines, which vary according to geographic location and environmental factors. Thus, outdoor studies are essential to understand the above and allow for early degradation detection to inform preventive measures.

In this study, we deployed $MAPbI_3$ TMS solar cells and mini modules in the humid climate of North Yorkshire (UK), monitoring their performance across different seasons. By testing various encapsulation strategies, we identified moisture as a key factor influencing device degradation, leading to an initial increase in open-circuit voltage, temporarily boosting power output. We found this V_{OC} response to be strongly correlated with relative humidity, which drove the formation and dissolution of $MAPbI_3$ monohydrate, initially facilitating charge extraction at the perovskite/carbon interface. While moderate hydrate formation was beneficial, exceeding a threshold concentration led to irreversible degradation. This could be prevented with the use of Parylene-C to encapsulate the device and limit water ingress. Remarkably, we demonstrated partial recovery of the devices through the application of temperature and vacuum treatments. Furthermore, our observations indicated that in humid environments, changes in V_{OC} with RH and shifts in short-circuit current serve as reliable indicators of hydrate formation or dissolution. These changes could provide early warning signals for *in situ* maintenance actions, helping to optimize device performance and extend their operational life.

Experimental section

Chemicals and materials

For the perovskite solution preparation gamma butyrolactone (GBL, Thermo Scientific Chemicals, 99+) and methanol (MeOH, Fisher Chemical, Extra Dry, for Synthesis) were used. The organic cation salt methylammonium iodide (MAI) and the additive 5-ammonium valeric acid iodide (AVAI) were purchased from Greatcell solar. The lead precursor PbI_2 (99.99%) was acquired from TCI chemicals. For device fabrication, carbon (Elcocarb B/SP) and zirconium oxide pastes (Zr-Nanoxide ZT/SP) were purchased from Solaronix. The mesoporous titanium dioxide paste (transparent) was acquired from Sigma Aldrich. For the deposition of the spray coated TiO_2 layer, acetylacetone (≥99.5%) and titanium(IV) isopropoxide were purchased from Sigma Aldrich. Absolute ethanol (99.8%) was acquired from Thermo Scientific.

All chemicals were used without further purification.

Solar cell and minimodule fabrication

Fluorine-doped tin oxide (FTO, Pilkington, 7 Ω sq^{-1}) coated glass substrates were prepared by brushing with a 2% Hellmanex in water solution followed by rinsing with de-ionised water, acetone, and ethanol. Each rinse was dried with a nitrogen flow and ozone cleaned for 15 minutes before subsequent layer depositions. A compact TiO_2 film was deposited using spray pyrolysis (15 cycles) on a hotplate at 450 °C with 3.6 ml of acetylacetone and 2.4 ml of titanium(IV) isopropoxide dissolved in 54 ml of ethanol. Afterwards, a mesoporous titania (m-TiO_2) film was screen printed using a polyester 165.31 mesh and sintered at 450 °C for 30 minutes. Substrates were laser etched (ULYXE DPSS laser marker) to separate contacts, followed by screen printing and sintering of mesoporous ZrO_2 at 500 °C. Then, a mesoporous carbon layer was applied by a doctor blade, and the complete stack was annealed at 400 °C. All sintering steps included a 30-minutes ramp-up, a 30-minutes annealing stage and natural cooling to room temperature. The mesoporous layer thicknesses averaged 1.53 μm for m-TiO_2, 2.32 μm for m-ZrO_2, and 15–20 μm for carbon. The differences in sizing and stacking between the layers for solar cells *versus* minimodules are highlighted in Fig. S1 in the ESI.† Maximum active area sizes for solar cells and minimodules were 0.96 cm^2 and 15 cm^2. However, due to the manual definition of top and bottom edges of the mesoporous layers with tape before screen printing the devices, variations in total length of the stripe occurred, normally reducing the active area size. The perovskite solution was prepared by following the protocol from Hashmi *et al.*[12]

Before stack-infiltration, the edges of the samples were coated with petroleum jelly to prevent the perovskite from coating the electrode contact area. The perovskite solution was

then infiltrated into the TMS solar cells and minimodules using slot-die coating (Ossila). Solar cells were deposited with a flow speed of 50 μl s^{-1} of solution at 12 mm s^{-1}, while minimodules 400 μl at 12 mm s^{-1}. Annealing was then conducted for 5 hours in air at 50 °C. Subsequently, a humidity treatment was performed in an enclosed atmosphere at 40 °C for 12 hours using a saturated binary salt solution (NaCl) to maintain around 75% RH.[13] The protective petroleum jelly was removed with acetone-soaked cotton buds and low-temperature carbon was deposited on the positive contact and dried at 100 °C for 10 minutes. Finally, silver paint was applied to both positive and negative contacts. The TMS solar cell sample made with recovered carbon black (rCB) was fabricated as described in previous work.[14]

Device encapsulation

Epoxy/glass encapsulation of devices used a two-part epoxy resin (Araldite, RS UK) around the edges of the carbon with a glass slide on top. Pressure was applied with clips until the resin reached its full strength after 2 hours.

For the POE/glass encapsulation, a square frame of polyolefin film was positioned around the edges of the mesoporous carbon in the minimodule and covered with a glass slide. Encapsulation was then performed in a Rise Core 1 semi-automatic flat plate laminator under the conditions detailed Table S1, ESI.†

The parylene-C deposition was performed in a SCS PDS 2010 coater under room temperature with a pressure set point of 3.3 Pa. Before the deposition, samples were placed within the vacuum chamber and a small quantity of adhesion promoter (AZ-174 Silane) was applied to the chamber walls.

Characterization

The X-ray diffraction (XRD) spectra were conducted on two Cu X-ray diffractometers: a Bruker D8 Advance and a Malvern PANalytical X'Pert Pro coupled with a temperature stage. Both were configured in a Bragg Brentano setup, where the k_β radiation was removed with a 0.2 Ni filter and the Cuα_2 stripped from the Cuα_1 ($\lambda = 1.5418$ Å) using the Rachinger method in the X'Pert Highscore Plus software. Raman measurements were taken with an Edinburgh Instruments RMS1000 multimodal confocal microscope. AFM images were acquired with a Park Systems XE-150.

The current density–voltage (J–V) characteristics of fabricated devices were measured at room temperature using an Ossila Source Meter under Air Mass 1.5 Global (AM 1.5G) with a factory calibrated Wavelabs SINUS-70 solar simulator intensity of 1 sun (100 mW cm^{-2}). The solar simulator includes an internal reference cell feedback system to test in plane monitor and spectrum during each single measurement multiple times. The light is uniform within the test area (51 × 51 mm) and the spectral match is Class A++ (0.95–1.05) with non-uniformity of irradiance of less than 2% (Class A). Full light coverage of the minimodules was ensured by placing them at the centre of the beam, considering that they have a non-photoactive 5 mm round edge. J–V scans were also taken at lower light intensities using the light intensity variation tool of the same solar simulator between 0.1 and 1 sun for reference against outdoor data. Speed of J–V scans was set at 0.1 V s^{-1} for both reverse and forward scans. Samples were covered with a 0.64 cm^2 vinyl mask in the case of the solar cells and custom cut vinyl masks with a target area size around 14.4 cm^2. Due to variations between active area sizes in the minimodules, adjustments were made to reach the areas noted in Table S2, ESI.† These variations were caused by the manual delimiting of the top and bottom edges of the stripes using tape before screen printing with the mesh.

For outdoor characterisation an in-house built system was used to measure J–V scans every hour during daylight hours (Ossila Source Meter Unit) and acquire environmental data as detailed in Section 2 of the ESI.†

Results and discussion

Device characteristics

Triple mesoscopic stack solar cells and minimodules were fabricated and encapsulated as described in the Experimental section, deployed, and tested outdoors at RAF Leeming (North Yorkshire, UK) during four different experiments between February and November 2024. Several encapsulation materials were used as summarized in Table 1, including the use of a 2-part epoxy resin (Araldite), a polyolefin sheet film (POE) and a CVD coated polymer thin film (Parylene-C). Samples were measured outdoors from sunrise to sunset on the days when measurements were conducted.

We note that the deployment period was longer than the measurement period, as detailed in Fig. S10 in the ESI.† Further details on the outdoor testing setup and data processing can be found in Sections 2 and 4 of the ESI.†

Table 1 Summary of outdoor deployed solar cells and minimodules by device type, encapsulation and deployment period

Exp. no.	Device type	Label	Encapsulation	Outdoor period
1	TMS, minimodule	SIP045-I	Epoxy/glass	15/02/2024 – 21/07/2024
2	TMS, solar cell, rCB	AN006-12L	Epoxy/glass	27/03/2024 – 29/05/2024
3	TMS, minimodule	AN014-04	POE/glass	01/08/2024 – 16/09/2024
	TMS, minimodule	AN014-06	POE/glass	
	TMS, minimodule	AN014-09	POE/glass	
	TMS, minimodule	AN014-12	None	
4	TMS, minimodule	SIP053-09	Parylene-C	15/11/2024 – 05/12/2024

We also note that several factors contributed to the modest efficiencies observed in this work compared to literature values (~15% for small cells, ~12% for minimodules).[2,3,15] These include cell aging prior to testing, fabrication-related challenges, and design limitations. Suboptimal conditions during manual printing, slot-die coating inconsistencies, and uneven temperature and airflow during annealing all affected performance. Additionally, large inter-stripe spacing in the minimodules limited voltage buildup. A detailed discussion of these effects, including specific device issues marked in Table S4† and supporting *J–V* data, is provided in Section 3 of the ESI.†

Outdoor conditions

The ambient conditions recorded in the measuring box highlighted two key weather factors at the outdoor location: low light intensity and high humidity. Low light conditions were particularly challenging for analysis due to the limitations of our solar simulator, as meaningful device performance assessments were only feasible above 0.1 sun. On average, 72.84% of measurements fell within the 0–0.1 suns range, varying significantly (even weekly) from a high of 90.96% in early March to a low of 57.28% in late March–early April (Fig. S10, ESI†). Despite the challenges posed by low light, we accounted for its impact in our analysis. However, for greater accuracy and reliability, we placed more emphasis on data collected above 0.1 sun, where performance assessments are more robust.

On the other hand, high humidity stands as the top influencing factor of device longevity, with over half (51.4%) of all daytime measurements exceeding 70% RH, fluctuating between 36.45% in late April and 74.94% in November–December. At night, RH was consistently higher, often nearing 100% at sunrise and sunset, as shown in Fig. S13–S20 in the ESI.† We also note that daytime humidity levels are likely to be even higher than recorded due to the overheating of the measuring box. The spikes registered in both cell and ambient temperature sensors were particularly pronounced in spring and summer when, despite historically higher rainfall, the number of rainy days was lower (Fig. S11, ESI†). As a result, prolonged sunny periods led to temperature peaks in the overheated box and a substantial reduction in relative humidity beyond typical expectations. In contrast, during November and December, over a third of the days were historically overcast, with rainfall volume remaining relatively low. Under these conditions, low light levels contributed to higher RH values, which were less affected by overheating, as insufficient sunlight prevented significant temperature increases.

Outdoor device response

Within this overall high humidity environment, the four experiments showed varying degrees of humidity impact, as illustrated in Fig. 1a, where drop icons indicate increasing sensitivity from Experiment 1 (least affected) to Experiment 4 (most affected). This classification is based on three factors: encapsulation architecture, encapsulation material, and seasonal weather conditions. Glass encapsulation in Experiments 1–3 minimized water ingress,[5] which primarily occurs at the edges, whereas Experiment 4, lacking glass, was the most affected.

The choice of encapsulation material also played a crucial role, with Parylene-C offering the highest resistance due to its hydrophobic, packed semi-crystalline structure, high-temperature stability, chemical resistance, and the full coverage of the device.[16–19] Epoxy resin, while presenting a strong cross-linked rigid structure successfully limiting water ingress,[20,21] becomes brittle above 80 °C,[5,22] making it more vulnerable; whereas the specific POE used, despite being more flexible and amorphous,[23] became even more susceptible to water ingress with temperature, since the melting point was located between 75–95 °C.[21,24] A summary of these material properties, including WVTR values and thermal degradation thresholds, is included in Table S1 in the ESI.†

Seasonal temperature variations further influenced degradation, particularly between April and September when overheating accelerated material breakdown. Experiment 1, using epoxy resin, experienced minimal impact at the beginning of the experiment, since the maximum cell temperature (T_{cell}) remains below 80 °C from February to April (Table S5, ESI†). Experiment 2, also with epoxy, reached maxima above 90 °C between April and May, increasing its susceptibility for degradation. Additionally, the use of recovered carbon black as a counter electrode drove more water through the structure compared with the virgin material as determined in previous research.[14] Experiment 3, using POE, faced similar high temperatures in August and September, making it even more fragile. Finally, Experiment 4, despite using the highly resistant Parylene-C, lacked glass protection and remained the most exposed to humidity, especially in cooler months when ambient and cell temperatures were lower.

Interestingly, in most experiments the power output of the cell initially improved relative to the baseline measurement before eventually decaying due to encapsulation failure (Fig. 1a). This improvement arose from an increase in open-circuit voltage, which correlated with moisture ingress and the formation and dissolution of $MAPbI_3$ hydrate under certain humidity levels. This process was confirmed through in-lab measurements and is discussed in detail later in this paper.

As such, in Experiment 1 the maximum V_{OC} was not reached until week 8 (early April), coinciding with the degradation of the epoxy resin due to high temperatures and the subsequent infiltration of moisture. In contrast, in Experiment 2, where temperatures exceed 90 °C from the outset, early epoxy failure allowed moisture infiltration, facilitated by rCB, leading to V_{OC} peaking within the first week. Similarly, in Experiment 3, high temperatures and the fragility of POE allowed water ingress from the beginning, resulting in an early increase in V_{OC}. In Experiment 4 rapid degradation was caused by immediate high moisture exposure, and a V_{OC} significantly higher than expected was recorded.

The hypothesis of hydrate formation and dissolution during outdoor experiments is further supported by Fig. 1b and c, where maximum power and V_{OC} are plotted against light intensity for Experiment 3, specifically for AN014-06 (POE-encapsulated) and AN014-12 (unencapsulated). The figures are

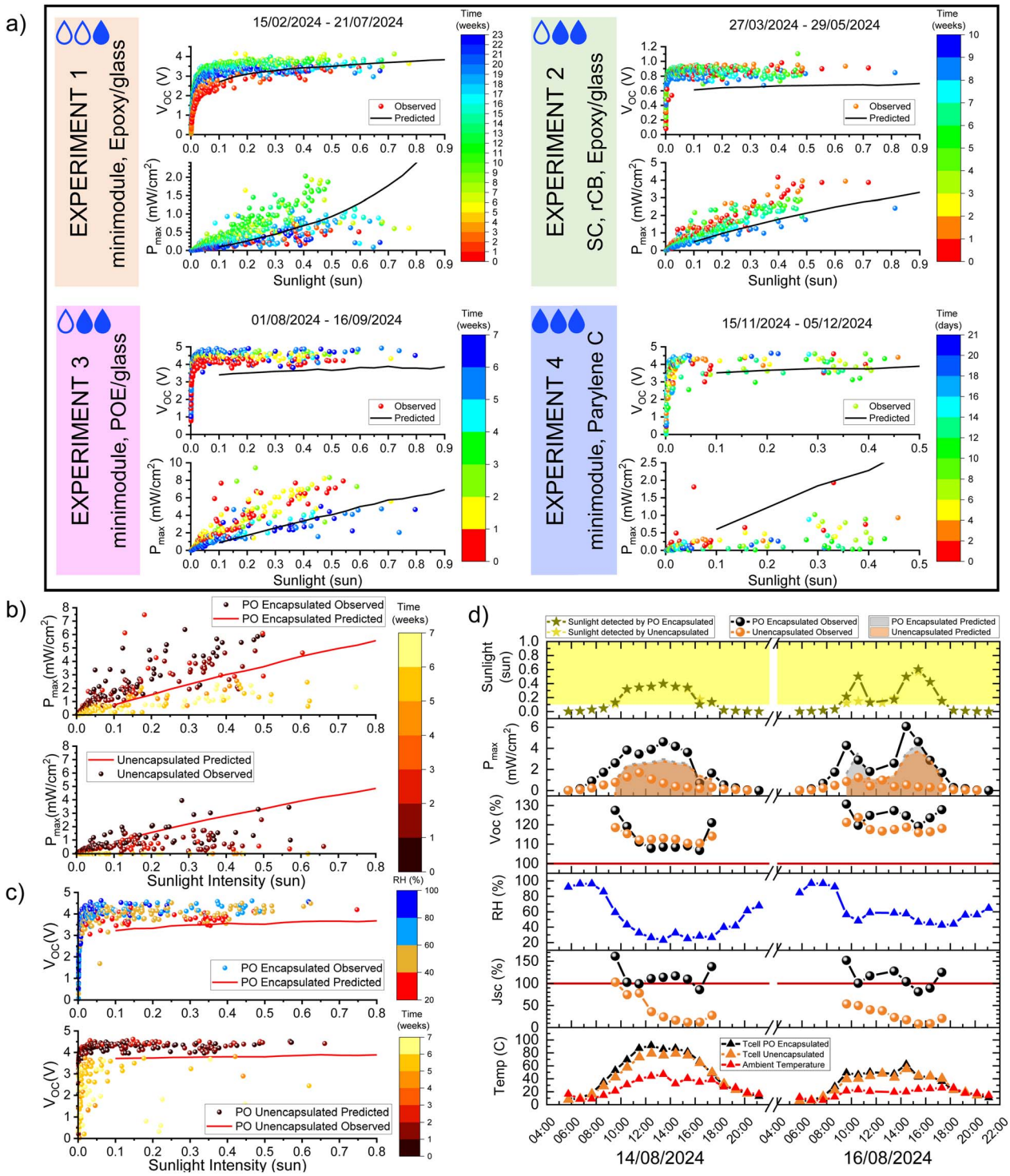

Fig. 1 (a) Maximum power (P_{max}) and V_{OC} plotted against sunlight intensity over time of minimodules deployed outdoors in Experiments 1 to 4, ordered from less to more affected by moisture. (b) P_{max} *versus* sunlight over time of POE encapsulated and unencapsulated TMS minimodules. (c) V_{OC} *versus* sunlight of POE encapsulated (AN014-06) and unencapsulated (AN014-12) TMS minimodules during outdoor Experiment 3, colour mapped against humidity (top) and time (bottom). (d) Evolution of P_{max}, V_{OC} and J_{SC} of POE encapsulated and unencapsulated TMS minimodules over the course of two days with environmental conditions. Note the V_{OC} and J_{SC} are plotted as the percentage of change compared to initial value.

color-mapped in two ways: one tracking time and the other RH levels experienced by the cells. In the encapsulated sample, where water ingress occurred more gradually than in the bare sample, V_{OC} varied strongly with RH rather than with time. Higher humidity levels prompted the formation of the perovskite monohydrate and raised the V_{OC}, while the dissolution of

the hydrate at lower RH levels dropped the V_{OC}. These results demonstrate the reversibility of the process. This pattern was also evident in the other experiments, as shown in Fig. S12 in the ESI.† The extent to which RH dominates V_{OC}, as opposed to time, corresponds to the rate at which hydrate can be formed and dissolved before irreversible degradation takes place (which is eventually visible with the passing of time). Experiments 2 and 3 exhibited the highest correlation between V_{OC} and RH, where elevated temperatures enabled the devices to shift between lower V_{OC} at lower RH (no hydrate) and higher V_{OC} at higher RH (more hydrate). In Experiment 1, this correlation only emerges after week 8, when temperature-induced epoxy failure allows moisture ingress, making time the dominant factor in early V_{OC} trends. In Experiment 4, the V_{OC}-to-RH correlation was also present but with fewer data points, given the rapid degradation process caused by higher humidity levels and lower temperatures.

This process was more clearly visible in the devices within the daily oscillations of RH and temperature, as depicted in Fig. 1d (but also found in Fig. S13–S20 in the ESI†). In Fig. 1d the daily evolution of V_{OC}, J_{SC} and P_{max} *versus* the original values for the POE-encapsulated (AN014-06) and bare TMS minimodules (AN014-12) are tracked for irradiances above 0.1 sun. On the left of the plot, data from the 14/08/24 was collected on a relatively sunny day with sparse interference of clouds, allowing both the surface cell and the ambient measuring box temperatures to rise significantly compared to the more intermittent illumination seen on 16/08/24. In both days V_{OC} traces oscillations in RH quite closely, especially in the encapsulated sample, pointing at the dissolution and formation of hydrate in pair with the observed ambient humidity. Interestingly, variations in the J_{SC} were dependent on the surface temperature, reflecting the different dynamics of the hydrate dissolution.

On the 14/08, J_{SC} in the POE-encapsulated sample changed in the opposite direction to the V_{OC}, particularly between 11:00 and 15:00, coinciding with peak temperatures above 80 °C. Here, the hydrate dissolved as RH decreased, dropping the V_{OC}.

Since the device surface temperature was high enough, the J_{SC} progressively recovered as water exited the stack and the perovskite grains recrystallised. On the other hand, on 16/08 maximum temperatures plateaued around 50 °C, with the J_{SC} following precisely the evolution of the V_{OC} and hence of the RH. The tracing of RH by V_{OC} and J_{SC} simultaneously was also observed under humid and cold weather conditions as displayed in Fig. S20, ESI.†

In-lab humidity and recovery experiments

To better understand the formation and dissolution of hydrates in outdoor conditions, we exposed TMS $MAPbI_3$ solar cells and minimodules to an indoor high-humidity environment (>90% RH) by enclosing them in a sealed box containing vials of deionized water. Some samples were left bare, while others were encapsulated with a 10 μm Parylene-C hydrophobic blanket layer, forming a pinhole-free film with no negative effects on the device performance, as highlighted in Section 5 of the ESI.† We note that although the successful use of Parylene-C as a film encapsulation on planar perovskites has already been demonstrated,[25,26] this work presents its efficacy on a triple mesoscopic stack architecture for the first time. This encapsulation slowed down the degradation process, allowing us to analyze its dynamics in relation to the cell parameters over time.

Table 2 Summary of in-lab tested solar cells and minimodules by device, encapsulation and treatment types

Label	Device type	Encapsulation	Treatment
AN013-11	Minimodule	Parylene-C	Hydration, LTR, VR
SIP053-03	Minimodule	Parylene-C	Hydration, LTR
AN012-a-03	Minimodule	None	Hydration
AN012-a-04	Minimodule	None	Hydration
SIP058-01	Solar cell	Parylene-C	Hydration, VR
SIP058-02	Solar cell	None	Hydration, VR
SIP058-04	Solar cell	Parylene-C	Hydration, HTR
SIP058-05	Solar cell	Parylene-C	Hydration, HTR
SIP058-12	Solar cell	None	Hydration, HTR

To aid the reader in navigating the sample nomenclature used throughout this section, Table 2 provides a summary of each device's name, encapsulation type (Parylene-C or none), and all the experimental conditions to which it was subjected: hydration, low-temperature recovery (LTR), high-temperature recovery (HTR), or vacuum recovery (VR). Note that all samples were fabricated using the same TMS perovskite recipe and that sample names follow a standard format where the prefix (*e.g.*, AN013, SIP053) indicates the user and fabrication batch, and the number after the hyphen identifies the specific device within that batch, as previously clarified in Section 3 of the ESI.† Like observations in the field, the minimodules exhibited an increase in open-circuit voltage relative to their initial values (Fig. 2a). This increase was significantly more pronounced in encapsulated devices, which showed a 20–30% rise, compared to just 5% in non-encapsulated samples. Additionally, the peak V_{OC} occurred later in encapsulated samples (48 hours) than in unencapsulated ones (24 hours), after which the latter began to decline. A comparable trend was observed in solar cells subjected to hydration for 24 hours, as shown in Fig. S22 in the ESI.† Encapsulated cells displayed a clear V_{OC} enhancement, whereas non-encapsulated samples suffered irreversible degradation, due to faster hydrate formation and the emergence of irreversible phases.

The evolution of the short-circuit current density varied across samples. Some exhibited an increase over time (SIP053-03, SIP058-04), while others showed a decrease (AN013-11, SIP058-01) or minimal change (SIP053-05). This variability is likely due to differences in hydration and degradation rates, which depend on the degree of moisture infiltration. Slight variations in the perovskite filling during fabrication may have led to differing levels of perovskite exposure to moisture, particularly in cases of overfilling or underfilling the carbon layers. Variation in the perovskite carbon filling affecting the morphology is shown in the AFM images in Section 6 of the ESI.† Additionally, differences in crystallization could have resulted in varying defect densities, creating more sites for

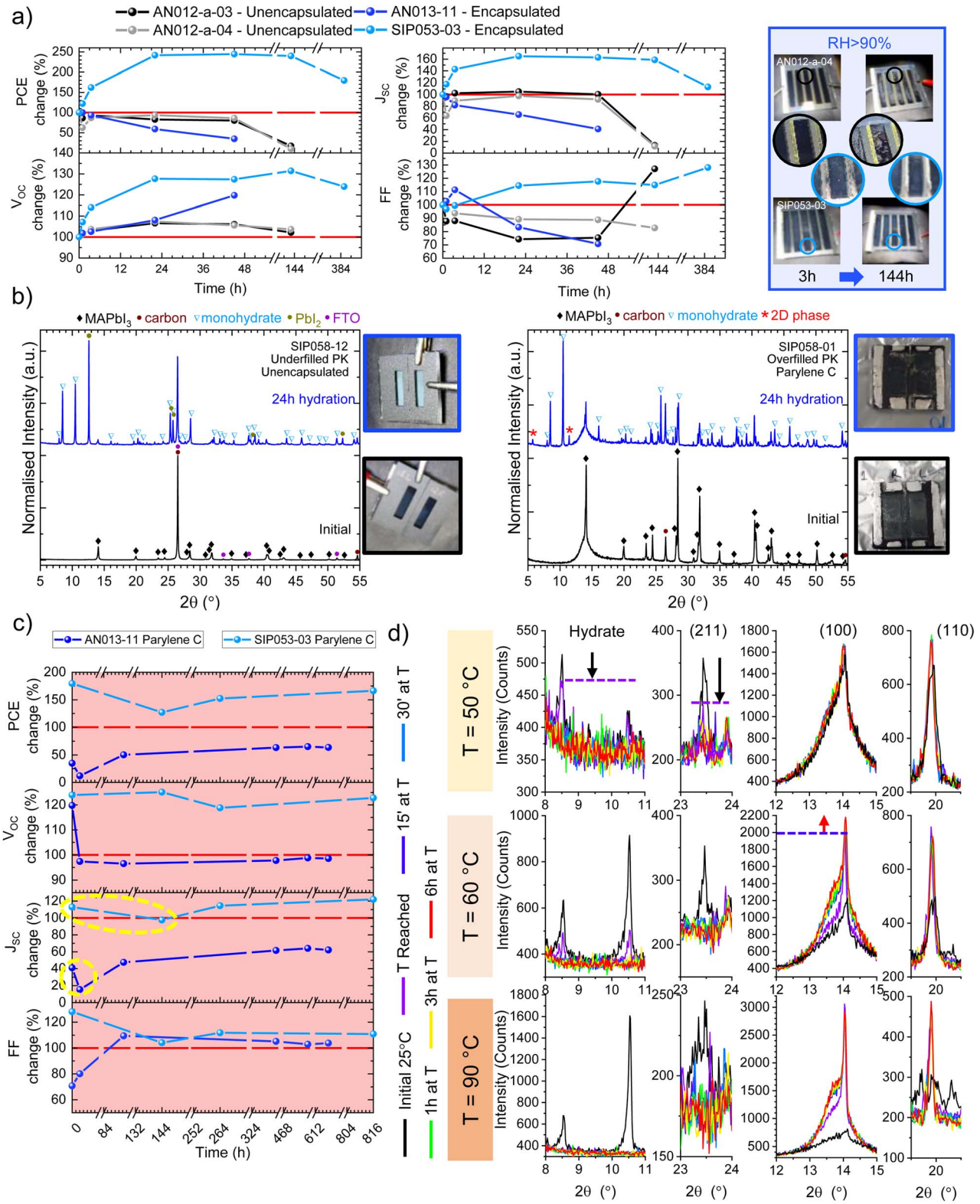

Fig. 2 (a) Variation of solar cell parameters (PCE, J_{SC}, V_{OC}, FF) *versus* initial values (in %) and images of unencapsulated and Parylene-C coated TMS minimodules exposed to high humidity (RH > 90%) for increasing times. (b) XRD scans and images of unencapsulated and Parylene-C coated TMS minimodules exposed to 24 h of hydration. (c) Variation of solar cell parameters (PCE, J_{SC}, V_{OC}, FF) *versus* initial values (in %) of hydrated Parylene-C TMS minimodules in a exposed to 40–50 °C for increasing times. (d) *In situ* temperature XRD scans of key perovskite planes performed on 3 Parylene-C coated TMS solar cells at 50 °C, 60 °C and 90 °C.

water penetration and accelerating degradation in some samples.[27]

The speed of the hydration process is clearly illustrated in the minimodule images (Fig. 2a) and the XRD scans of the solar cells (Fig. 2b), which follow the dynamics of eqn (1), as described in the literature.[28] Upon hydration, $MAPbI_3$ undergoes a visible color change from dark brown to transparent. This transformation is considered partially reversible, as both the monohydrate ($[MAPbI_3 \cdot H_2O]$) and dihydrate ($[MA_4PbI_6 \cdot 2H_2O]$) phases can revert to polycrystalline $MAPbI_3$. However, once water molecules saturate the structure and displace the MA cation, the process becomes irreversible, leading to the formation of yellow PbI_2. Eventually, when the entire film is converted, excess water can dissolve MA, causing irreversible structural degradation.[28]

$$4\ MAPbI_3 + 4H_2O \leftrightarrow \underbrace{4[MAPbI_3 \cdot H_2O]}_{\text{monohydrate}} \leftrightarrow \underbrace{[MA_4PbI_6 \cdot 2H_2O]}_{\text{dihydrate}} + 3PbI_2 + 2H_2O \quad (1)$$

Eqn (1) $MAPbI_3$ hydration reaction.

In the case of the minimodules (Fig. 2a), encapsulated devices predominantly exhibited the formation of transparent hydrate crystals, whereas unencapsulated samples showed distinct yellow PbI_2 spots, indicating a faster reaction rate. Similarly, after 24 hours of hydration, both encapsulated and non-encapsulated TMS solar cells developed the monohydrate phase. However, only the non-Parylene samples displayed PbI_2, as revealed by the XRD scans in Fig. 2b and S21 from the ESI,† making the degradation irreversible.

The volume of infiltrated perovskite also played a distinctive role in the speed of hydration behaviour which can be tracked by comparing the intensity ratio of the $MAPbI_3$ (110) plane at 14.1° to the carbon peak at 26.5°. Samples SIP058-01 (Fig. 2b) and SIP058-02 (Fig. S21 ESI†) contained a thicker perovskite layer extending beyond the carbon height due to excess flow of perovskite precursor solution during the slot-die coating process compared to samples SIP058-12 (Fig. 2b) and SIP058-04 (Fig. S21 ESI†). A more pronounced carbon peak can be seen in the latter samples, consistent with a lower perovskite content.

This variation significantly influenced hydration dynamics: in overfilled samples, water rapidly percolated through, accelerating the conversion of perovskite into its hydrated form. Conversely, samples better protected by the carbon layer showed greater resistance to water ingress, as evidenced by the stronger perovskite peaks in their XRD patterns post-hydration. Notably, in SIP058-02 (Fig. S21, ESI†), the $MAPbI_3$ phases vanished entirely from the diffraction pattern.

Interestingly, the faster hydration experienced by the Parylene-C coated overfilled sample (SIP058-01), led to the emergence of two distinct peaks at 5.76° and 11.44° (Fig. 2b). These do not correspond to typical monohydrate or dihydrate phases. The low-angle position of the first peak suggests the formation of a 2D perovskite phase, potentially facilitated by the AVA cation, similarly to what is observed in other Ruddlesden-Popper perovskites made with bulky cations like BA or DMC.[29,30] Remarkably, the Parylene-C layer effectively prevented the escape of the MA cation, inhibiting irreversible PbI_2 formation—an effect that was also later confirmed during the temperature recovery treatment.

After hydration, we subjected the minimodules and solar cells to temperature recovery, mirroring the conditions observed in the field. As shown in Fig. 2c and S24 (ESI),† the Parylene-C-coated minimodules were placed in an oven at a relatively low temperature (40–50 °C) for up to 618 and 816 hours following the hydration recorded in Fig. 2a. While AN013-11 exhibited a drop in voltage as expected due to hydrate dissolution, SIP053-03 had already begun to lose V_{OC} during the hydration stage (Fig. 2a). Consequently, when subjected to heat, it did not show an immediate further drop, suggesting that degradation had already progressed too far for effective recovery.

In contrast, both the AN013-11 minimodule and solar cells exposed to higher temperature (90 °C, Fig. S25a, ESI†) exhibited the expected V_{OC} drop compared to the hydrated stage.

Notably, the J_{SC} behavior aligns with field observations when cell temperatures remained below 50–60 °C: before any recovery occurs, an initial drop in short-circuit current is observed (Fig. 2c). On the other hand, when hydrated solar cells were directly exposed to a high temperature (90 °C) for an extended period (3 h and 24 h)—longer than in field conditions—J_{SC} decreased. We attribute this to accelerated recrystallization, as evidenced in Fig. S25 (ESI).† We hypothesize this discrepancy was caused by differences in exposure time and hydration levels. In the field, water ingress in POE/glass-encapsulated samples (Fig. 1b and c) was slower than in our indoor Parylene-C-coated samples due to the protective glass layer. As a result, field samples may have contained fewer hydrated crystals. Additionally, the fluctuating nature of outdoor sunlight (*e.g.*, cloud cover) may have limited their exposure to high temperatures, possibly to a shorter duration than our first controlled measurement at 3 hours. As such, the recrystallisation process might have underfilled the pores, causing a decrease in the solar cell performance. Crucially, despite high-temperature exposure, the Parylene-C coating effectively prevented PbI_2 formation (Fig. S25c, ESI†), demonstrating its dual role as an effective encapsulation layer—both in limiting water ingress and in inhibiting MA cation loss, whether through water dissolution or temperature exposure.

To gain a deeper understanding of the dehydration process at different temperatures, we conducted *in situ* XRD measurements over time on three hydrated Parylene-C encapsulated solar cells. The results, shown in Fig. 2d, correspond to temperatures of 50 °C, 60 °C, and 90 °C. These temperatures were chosen to observe the dynamics both below and above the phase transition temperature of $MAPbI_3$, which occurs around 55–57 °C.[31,32] The hydration levels varied across the samples, with the 50 °C sample containing less hydrate than the 60 °C sample, and the 60 °C sample containing less than the 90 °C sample, despite all being hydrated for the same duration (48 hours) due to sample-to-sample differences.

In Fig. 2d, we compared the evolution of four XRD peaks with temperature: the monohydrate peaks between 8° and 11°, the (211) $MAPbI_3$ tetragonal peak, the main $MAPbI_3$ peak around 14° (which can be tetragonal (110) or cubic (100)), and the $MAPbI_3$ peak around 20° ((110) in tetragonal, (200) in cubic). Each sample was initially scanned at room temperature (25 °C) and scanned again when their respective temperature targets were reached in a few minutes. Then, samples were kept at these temperatures and measured at increasing intervals: 15 minutes, 30 minutes, 1 hour, 3 hours, and 6 hours.

The results from the sample exposed to 50 °C revealed a clear relationship between the dissolution of the hydrate phases and the disappearance of the tetragonal peak. The XRD scan taken after reaching 50 °C shows a drop in both the hydrate peaks and the tetragonal peak. This suggests that the perovskite at that stage was a mix of both cubic and tetragonal phases. We hypothesize that the dissolution of the hydrate is triggered by the $MAPbI_3$ structure expelling the water molecules out as it transitions from tetragonal to cubic. After 15 minutes, this transition was complete: the tetragonal peak disappeared, and the hydrate phases were no longer present. A similar process occurred at 60 °C and 90 °C. When 60 °C were reached, the cubic phase was fully transformed in the scanned area, with some remnants of the hydrate still present, which disappeared after 15 minutes. After reaching 90 °C, the phase transition was fully completed at a macroscopic level, with the two hydrate peaks between 8° and 11° completely vanished.

Regarding recrystallization, we observed that after the initial 15-minutes period, which transformed the tetragonal phase to cubic, there was minimal change in the (100) and (110) $MAPbI_3$ cubic peaks at 50 °C. At 60 °C, recrystallization had begun, shown by the growth of the (100) peak between the 15-minutes and 6-hours exposures. This suggests that water did not immediately leave the stack after hydrate dissolution; instead, it likely remained around the grain boundaries since this is where the hydrate tends to form,[33] progressively leaving over time and temperature, facilitating recrystallization. A similar trend was observed in Fig. S25 and Table S6 in the ESI.† Here, some of the solar cells (SIP058-05 and SIP058-12) experienced weight loss between 3 and 24 hours of high-temperature exposure, which coincided with a change in the $MAPbI_3$ (200)/(110) ratio, indicating the evaporation of water and recrystallization of the perovskite. Note that, while the samples were exposed to high temperatures in an oven, the XRD measurements were taken at room temperature (not *in situ*), so the tetragonal phases were discussed here.

Interestingly, the *in situ* XRD measurement at 90 °C shows the main perovskite peak initially dropping between reaching the target temperature and the 30-minutes mark, then increasing again by the 6-hours point (Fig. S26, ESI†). We anticipate that, due to the high temperature, water exited the stack much faster than in the other cases, which likely altered the crystallization dynamics and the final shape and crystallinity of the perovskite.

Based on the evidence presented above, we have developed a hypothesis for the step-by-step hydration–dehydration mechanism, illustrated in Fig. 3a, starting with a fresh device (step 1). When a $MAPbI_3$ TMS device is exposed to high humidity, water progressively percolates through the structure, initiating the formation of the hydrate phase from the carbon layer down into the material (step 2). We assume this route is the preferred one, given that there is more exposed surface area on the top of the sample than on the sides, facilitating greater water ingress from the top. The formed hydrate might present a valence band with an intermediate energy level between that of the $MAPbI_3$ and the carbon, closing the existing gap between them, similarly to what occurs in planar architectures, with Spiro-OMeTAD and gold.[2] The existence of an intermediate valence band can explain the increase in open-circuit voltage as charge extraction improves, while also initially boosting the short-circuit current.

As hydration continues deeper into the structure (step 3), shunts may form when the hydrate, which is known to have higher conductivity than $MAPbI_3$,[34] puts both the TiO_2 and carbon layers into contact, dropping the J_{SC}. The V_{OC} may continue to rise during this stage, as more hydrate is formed in the carbon layer, which is the thickest and contains the most perovskite. However, as the black $MAPbI_3$ phase transforms into the transparent, non-photoactive hydrate phase, the J_{SC} decreases due to the reduced amount of light-active material within the same area. This is evident when observing the shape of the *J–V* scans of both cells and minimodules when hydrated, which resemble the shapes of partial light shading in devices (Fig. S22 and S23a, ESI†).

As hydration progresses further and fully transforms the perovskite into hydrate and other irreversible phases, both J_{SC} and V_{OC} drop due to the absence of photoactive material (step 4). While the exact limit for effective recovery is still unclear from our experiments, we hypothesize that this could be placed within the early stages of hydration (steps 1–2), where the hydrate remains confined mostly within the carbon layer. This is because the presence of water deep within the structure might have detrimental effects, such as lifting the TiO_2 layer,[35] or hindering proper recrystallization of the perovskite within the pores.

Recovery can be triggered by heating the device above the perovskite transition temperature (step a), which facilitates the release of water molecules from the crystalline hydrate arrangement into an amorphous state, potentially within the grain boundaries,[33] while dropping the V_{OC}. The presence of water at the grain boundaries limits current flow, dropping the J_{SC}. At higher temperatures, this process occurs more quickly, leading to a faster recovery of J_{SC}, while lower temperatures require more time for recrystallization to take place.

In addition to temperature recovery, we investigated the use of vacuum as a method for removing the hydrate. To assess this, we rehydrated the Parylene-coated minimodule (AN013-11) by exposing it to 24 h of high humidity, equivalent to the already hydrated solar cell (SIP058-01). Subsequently, the samples were placed in a vacuum desiccator at room temperature for durations of 534 hours and 23 hours, respectively, as shown in Fig. 3b and S27, ESI.† Both samples exhibited a decrease in V_{OC} during the vacuum treatment. For SIP058-01, this reduction in V_{OC} was accompanied by a progressive decrease in hydrate presence, as evidenced by the XRD data (Fig. 3c), with residual

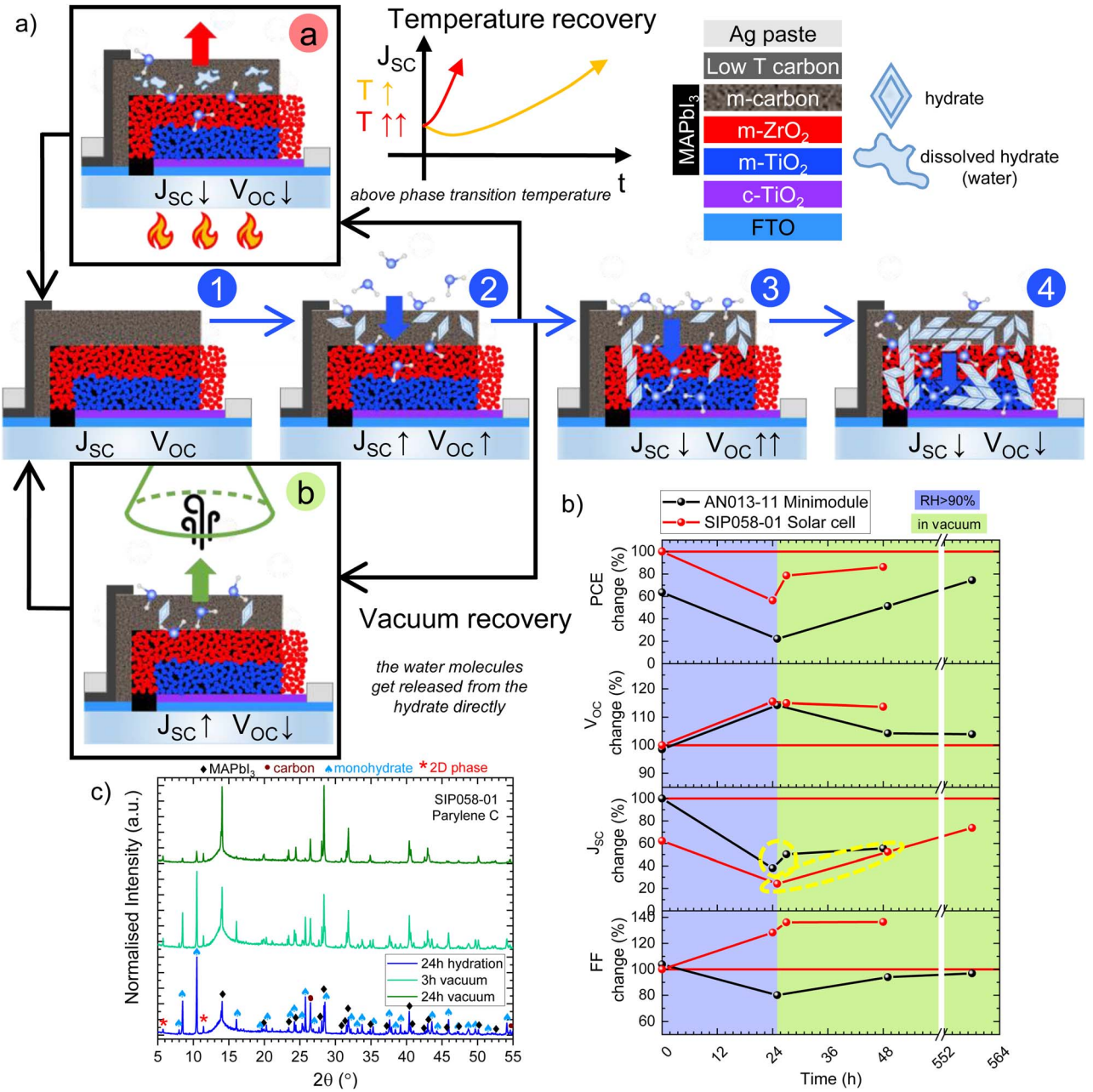

Fig. 3 (a) Diagram for the proposed hydration (steps 1–4) and recovery mechanism (step a and b) of perovskite TMS devices exposed to high humidity levels. (b) Variation of solar cell parameters (PCE, J_{SC}, V_{OC}, FF) *versus* initial values (in %) of Parylene-C coated TMS devices exposed to high humidity (RH > 90%) for 24 h and exposed to vacuum at increasing times. (c) XRD scans of Parylene-C coated TMS solar cell exposed to 24 h of hydration followed by 3 h and 24 h under vacuum.

hydrate remaining in the sample after 24 hours. Interestingly, unlike the temperature recovery treatment, the J_{SC} did not experience a decline; rather, it showed an immediate improvement. Since the treatment was performed at room temperature and $MAPbI_3$ remained in a predominantly tetragonal phase, we hypothesize the water did not undergo a transition into an amorphous arrangement. Instead, the hydrate was gradually removed from its crystalline form *via* water extraction by the vacuum (Fig. 3a, step b). This recovery process resulted in a restoration of 74.4% of the original performance for AN013-11 after 534 hours, significantly outperforming the 63.6% recovery observed with the temperature treatment after 816 hours. Based on these findings, we suggest that a combination of both recovery methods, when applied appropriately, may offer the most effective means of recovery.

The presence of an intermediate valence band in the hydrate remains difficult to conclusively prove due to the inherent instability of the material. Key measurements, such as X-ray photoelectron spectroscopy (XPS), which could provide valuable insights into this hypothesis, face significant challenges. First, XPS requires a vacuum environment, which would remove the water from the sample and dissolve the hydrate. Second, the

X-rays used in XPS analysis can slightly heat the sample, which may further dissolve any potentially remaining hydrate, complicating its detection. Finally, the use of a protective barrier such as Parylene-C to slow down the dehydration process and preserve the hydrate for a longer time, would render the XPS measurement ineffective. Since XPS is surface-sensitive, the X-rays would not penetrate the 10-micron thick Parylene-C layer to reach and analyze the hydrate beneath it, preventing accurate measurements.

Despite these challenges in measurement, our findings support the hypothesis that the presence of the hydrate is responsible for the observed increase in open circuit voltage (V_{OC}) upon hydration. Furthermore, we observed a consistent decrease in V_{OC} as the sample dehydrated. While the solar cells and minimodules tested in this study exhibited relatively modest performance, with power conversion efficiencies (PCEs) ranging from 2% to 8% under 1 sun, all samples displayed the same behavior: an increase in V_{OC} in response to hydration and a subsequent decrease in V_{OC} as dehydration occurred.

As such, the oscillating behaviour of V_{OC} provided a clear proxy for hydrate dynamics, yet the long-term degradation under the studied conditions was ultimately governed by the degree of moisture ingress. This is primarily dictated by the encapsulation architecture (*e.g.*, edge seal *vs.* full coverage, use of glass), the material's intrinsic properties, and the environmental conditions, especially temperature and humidity. Although device-specific factors like perovskite thickness or carbon layer uniformity influence how moisture spreads internally, these are secondary: if moisture is effectively excluded, degradation *via* hydrate formation is largely avoided. Thus, while fabrication quality affects the rate of failure, it is encapsulation performance under real-world stress that enables degradation. These findings highlight the need to jointly optimize both encapsulation and fabrication for robust, long-term stability.

Importantly, the indoor experiments successfully replicated and clarified key trends observed outdoors. In addition to the V_{OC}–RH relationship, they highlighted the role of temperature fluctuations in driving hydrate dissolution and influencing the J_{SC} response. Specifically, outdoor data showed contrasting J_{SC} behaviour at different cell temperatures: a drop at ~60 °C and a recovery at ~90 °C. In the lab, temperature recovery experiments on previously hydrated samples, supported by *in situ* XRD, revealed hydrate dissolution occurring near the perovskite phase transition (~55 °C). At moderate temperatures (40–60 °C), this process was accompanied by an initial drop in J_{SC} due to hydrate breakdown occurring before full perovskite recrystallization, consistent with the outdoor response at ~60 °C. At higher temperatures (~90 °C), faster water expulsion promoted quicker perovskite recrystallization and thus more rapid J_{SC} recovery, explaining the outdoor behaviour under those conditions.

Future work should build on our current findings by characterizing devices under low-light conditions, particularly below 0.1 sun, using neutral density filters. This would allow for a more detailed assessment of the outdoor performance in the low-light range, which represents a significant portion of the dataset for the northern UK climate. Likewise, the use of MPPT could provide more insight into the dynamic formation or dissolution of the hydrate under operating conditions. Additionally, this research could be the basis for the development of an outdoor testing system with integrated recovery methods, such as vacuum and a controllable passive heating system. Given our previous observations—where the greenhouse effect within the measurement box may have contributed to device recovery—these approaches could be applied more deliberately to mitigate hydrate formation and potentially extend device longevity. Further improvements in stability should also be explored through enhanced moisture barriers, including stronger side sealants, glass encapsulation, and a Parylene-C interlayer in TMS devices.

Conclusions

In this study, we demonstrated that in a highly humid outdoor environment (North Yorkshire, UK), the hydration of $MAPbI_3$ TMS perovskite solar cells and mini-modules leads to an initial increase in open-circuit voltage, temporarily improving the power output. This V_{OC} response correlates with relative humidity levels, rising with high RH and dropping with low RH. Through laboratory experiments, we confirmed that this V_{OC}-to-RH relationship is driven by the formation and dissolution of the $MAPbI_3$ monohydrate, which likely acts as an intermediate step in the valence band at the perovskite/carbon interface, facilitating charge extraction. We reproduced the V_{OC}-to-RH oscillations observed in the field and proposed a mechanism: high humidity triggers hydrate formation, raising V_{OC}. On the other hand, increased temperature above the $MAPbI_3$ phase transition temperature causes hydrate dissolution and water presence within the grain boundaries, that can progressively get expelled through recrystallisation. Additionally, we demonstrated that a vacuum treatment can also recover the perovskite by removing water directly from the hydrated lattice. We also found that Parylene-C encapsulation is highly effective, preventing irreversible degradation both under high humidity and high temperature environments. These discoveries are of paramount importance because they provide a means of detecting early, recoverable degradation in TMS $MAPbI_3$ perovskite devices before power loss occurs. This ability enables the timely application of recovery measures, in line with the principles of circular economy, to mitigate degradation *in situ*. Crucially, our observations were made under real outdoor conditions, which further validates the practical applicability of this approach. By detecting recoverable degradation early, we can implement corrective measures before significant power loss, working in conjunction with effective encapsulants to significantly extend the lifespan of TMS perovskite modules. This, in turn, can help drive the commercialization of these devices by improving their durability and raising their technology readiness level (TRL).

Data availability

The data supporting this article have been included as part of the ESI.† More raw data are available from the corresponding author on reasonable request.

Author contributions

SIP: conceptualization, data curation (outdoor device data processing), formal analysis (outdoor and indoor device data), investigation (device fabrication, encapsulation, and characterisation), methodology (design and construction of outdoor testing rig), software (software development for testing rig and data analysis), supervision (summer student), validation (in lab humidity tests, XRD, Raman), visualization (creation of figures and tables), writing – original draft. AN: investigation (device fabrication, encapsulation, and characterisation), supervision (summer student). MB: Resources (parylene-C deposition). JG: investigation (AFM measurements). EAG: conceptualization, funding acquisition, project administration, supervision, writing – review & editing.

Conflicts of interest

There are no conflicts to declare.

Acknowledgements

The temperature dependent XRD measurements were carried out by Tanzeela Anis at the Crystallography facility at Newcastle University. Ewan Förster contributed to the POE encapsulation under AN and SIP guidance. We thank the Defence Innovation Fund TLB Ideas Scheme (ViTAL Living Lab, 61182036) for enabling the outdoor testing. We thank Wastefront for providing the rCB. We thank the UKRI NICER programme for a flexible fund to initiate the collaboration and Newcastle University's EPSRC IAA Innovation to Impact fund.

Notes and references

1 National Renewable Energy Laboratory (NREL), *Interactive Best Research-Cell Efficiency Chart*, **https://www.nrel.gov/pv/interactive-cell-efficiency.html**, accessed 10 March 2025.
2 S. M. P. Meroni, C. Worsley, D. Raptis and T. M. Watson, *Energies*, 2021, **14**, 386.
3 W. Shao, J. He, J. He, D. Ma, J. Sheng, J. Liu and W. Wu, *Sol. RRL*, 2023, **7**, 2300623.
4 M. Xu, W. Ji, Y. Sheng, Y. Wu, H. Cheng, J. Meng, Z. Yan, J. Xu, A. Mei, Y. Hu, Y. Rong and H. Han, *Nano Energy*, 2020, **74**, 104842.
5 Y. Wang, I. Ahmad, T. Leung, J. Lin, W. Chen, F. Liu, A. M. C. Ng, Y. Zhang and A. B. Djurišić, *ACS Mater. Au*, 2022, **2**, 215–236.
6 Scott Lyon, Office of Engineering Communications Princeton University, Once seen as fleeting, a new solar tech proves its lasting power, **https://www.princeton.edu/news/2022/06/29/once-seen-fleeting-new-solar-tech-proves-its-lasting-power**, accessed 10 March 2025.
7 X. Zhao, T. Liu, Q. C. Burlingame, T. Liu, R. Holley, G. Cheng, N. Yao, F. Gao and Y.-L. Loo, *Science*, 2022, **377**, 307–310.
8 S. Pescetelli, A. Agresti, G. Viskadouros, S. Razza, K. Rogdakis, I. Kalogerakis, E. Spiliarotis, E. Leonardi, P. Mariani, L. Sorbello, M. Pierro, C. Cornaro, S. Bellani, L. Najafi, B. Martín-García, A. E. Del Rio Castillo, R. Oropesa-Nuñez, M. Prato, S. Maranghi, M. L. Parisi, A. Sinicropi, R. Basosi, F. Bonaccorso, E. Kymakis and A. Di Carlo, *Nat. Energy*, 2022, **7**, 597–607.
9 M. De Bastiani, E. Van Kerschaver, Q. Jeangros, A. Ur Rehman, E. Aydin, F. H. Isikgor, A. J. Mirabelli, M. Babics, J. Liu, S. Zhumagali, E. Ugur, G. T. Harrison, T. G. Allen, B. Chen, Y. Hou, S. Shikin, E. H. Sargent, C. Ballif, M. Salvador and S. De Wolf, *ACS Energy Lett.*, 2021, **6**, 2944–2951.
10 M. Babics, M. De Bastiani, E. Ugur, L. Xu, H. Bristow, F. Toniolo, W. Raja, A. S. Subbiah, J. Liu, L. V. Torres Merino, E. Aydin, S. Sarwade, T. G. Allen, A. Razzaq, N. Wehbe, M. F. Salvador and S. De Wolf, *Cell Rep. Phys. Sci.*, 2023, **4**, 101280.
11 Q. Emery, M. Remec, G. Paramasivam, S. Janke, J. Dagar, C. Ulbrich, R. Schlatmann, B. Stannowski, E. Unger and M. Khenkin, *ACS Appl. Mater. Interfaces*, 2022, **14**, 5159–5167.
12 S. G. Hashmi, D. Martineau, M. I. Dar, T. T. T. Myllymäki, T. Sarikka, V. Ulla, S. M. Zakeeruddin and M. Grätzel, *J. Mater. Chem. A*, 2017, **5**, 12060–12067.
13 L. Greenspan, *J. Res. Natl. Bur. Stand. A Phys. Chem.*, 1977, **81A**, 89.
14 S. Iglesias-Porras, A. Neild, L. Stevens, W. Li, C. Snape, O. Woodford, N. Straughan and E. A. Gibson, *ACS Sustainable Resour. Manage.*, 2025, **2**, 322–333.
15 M. Xu, W. Ji, Y. Sheng, Y. Wu, H. Cheng, J. Meng, Z. Yan, J. Xu, A. Mei, Y. Hu, Y. Rong and H. Han, *Nano Energy*, 2020, **74**, 104842.
16 B. Hou, Y. E. Lee, D. H. Kim, H. Ye, H. Kwon and S. H. Kim, *Macromol. Res.*, 2025, **33**, 185–194.
17 S. Buchwalder, A. Borzì, J. Diaz Leon, F. Bourgeois, C. Nicolier, S. Nicolay, A. Neels, O. Zywitzki, A. Hogg and J. Burger, *Polymers*, 2022, **14**, 3677.
18 SCS Speciality Coating Systems, *Does Parylene make my Product Waterproof?*, **https://scscoatings.com/newsroom/blog/does-parylene-make-my-product-waterproof/#:~:text=February16%2C2021,Chaoticweather**, accessed 1 July 2025.
19 SCS Specialty Coating Systems, *A Guide to Parylene Service Temperatures*, **https://scscoatings.com/newsroom/blog/a-guide-to-parylene-service-temperatures/#:~:text=Becauseoxygen%2Dfreeenvironmentsprohibit,tousingmajorParylenetypes.**, accessed 1 July 2025.
20 J. Yin, J. Cui, H. Zhou, S. Cui, C. Wang, J. Guo, J. Wei and X. Zhang, *Energy Technol.*, 2020, **8**, 2000513.
21 M. Babin, G. C. Eder, Y. Voronko and G. Oreski, *J. Appl. Polym. Sci.*, 2024, **141**(31), e55733.
22 *Araldite Rapid Syringe Epoxy|NWT4471P|Glues & Adhesives*, **https://www.officestationery.co.uk/product/araldite-rapid-syringe-epoxy-adhesive-24ml-pack-6-nwt4471p-NWT4471P/**, accessed 12 March 2025.
23 H. Jiao, M. Hegde, N. Li, M. Owen-Bellini, L. Schelhas, T. J. Dingemans and J. Huang, *PRX Energy*, 2024, **3**, 023013.
24 The Compound Company, *SAFETY DATA SHEET: Yparex - Silane Functionalised Polymer Film*, 2021.

25 H. Kim, J. Lee, B. Kim, H. R. Byun, S. H. Kim, H. M. Oh, S. Baik and M. S. Jeong, *Sci. Rep.*, 2019, **9**, 15461.
26 E. Ghahremani Rad, A. T. Gidey, T. Chowdhury and A. R. Uhl, Advancing Operational Stability of Inverted Perovskite Solar Cells Utilizing Parylene-C Encapsulation Techniques, *Oral presentation, Proceedings of the International Conference on Hybrid and Organic Photovoltaics (HOPV24)*, Valencia, Spain, 2024, DOI: **10.29363/nanoge.hopv.2024.129**.
27 W. Chi and S. K. Banerjee, *Chem. Mater.*, 2021, **33**, 4269–4303.
28 A. M. A. Leguy, Y. Hu, M. Campoy-Quiles, M. I. Alonso, O. J. Weber, P. Azarhoosh, M. van Schilfgaarde, M. T. Weller, T. Bein, J. Nelson, P. Docampo and P. R. F. Barnes, *Chem. Mater.*, 2015, **27**, 3397–3407.
29 A. A. Zhumekenov, Y. Li, Y. Zhou, N. Yantara, A. Kanwat, B. Febriansyah, D. J. J. Tay, H. R. Abuzeid, Y. B. Tay, E. B. Miftahullatif, K. Hippalgaonkar, S. A. Pullarkat, J. Yin and N. Mathews, *J. Am. Chem. Soc.*, 2024, **146**, 6706–6720.
30 C. C. Stoumpos, D. H. Cao, D. J. Clark, J. Young, J. M. Rondinelli, J. I. Jang, J. T. Hupp and M. G. Kanatzidis, *Chem. Mater.*, 2016, **28**, 2852–2867.
31 F. Lehmann, A. Franz, D. M. Többens, S. Levcenco, T. Unold, A. Taubert and S. Schorr, *RSC Adv.*, 2019, **9**, 11151–11159.
32 P. S. Whitfield, N. Herron, W. E. Guise, K. Page, Y. Q. Cheng, I. Milas and M. K. Crawford, *Sci. Rep.*, 2016, **6**, 35685.
33 D. Li, S. A. Bretschneider, V. W. Bergmann, I. M. Hermes, J. Mars, A. Klasen, H. Lu, W. Tremel, M. Mezger, H.-J. Butt, S. A. L. Weber and R. Berger, *J. Phys. Chem. C*, 2016, **120**, 6363–6368.
34 X. Zhao, Y. Sun, S. Liu, G. Chen, P. Chen, J. Wang, W. Cao and C. Wang, *Nanomaterials*, 2022, **12**, 523.
35 A. Eichler-Volf, L. Xue, G. Dornberg, H. Chen, A. Kovalev, D. Enke, Y. Wang, E. V. Gorb, S. N. Gorb and M. Steinhart, *ACS Appl. Mater. Interfaces*, 2016, **8**, 22593–22604.